Hall coefficient and resistivity in the doped bilayer Hubbard model

Yin Shi [1,*] Jonathan Schirmer,[2,†] and Long-Qing Chen[1]

[1]*Department of Materials Science and Engineering, The Pennsylvania State University, University Park, Pennsylvania 16802, USA*

[2]*Department of Physics, The Pennsylvania State University, University Park, Pennsylvania 16802, USA*

(Received 23 August 2023; revised 21 January 2024; accepted 23 January 2024; published 7 February 2024)

Finding and understanding non-Fermi-liquid transport behaviors are at the core of condensed matter physics. Most of the existing studies in this field were devoted to the monolayer Hubbard model, which is the minimal model that captures the essential features of high-temperature superconductivity. Here, we discover another type of non-Fermi-liquid behavior emergent in the hole-doped bilayer Hubbard model, using dynamical mean-field theory with a full consideration of the short-range interlayer electron correlation. We find that at low temperatures, the Hall coefficient has a strong nonmonotonic dependence on temperature, leading to a double or quadruple reversal of its sign depending on the doping level. At the same time, the resistivity exhibits two plateaus rather than linearity in its temperature dependence. We show that these intriguing transport behaviors stem from the formation of coherent interlayer singlets, which scatter off gapped collective modes arising from short-range interlayer antiferromagnetic fluctuations.

DOI: 10.1103/PhysRevB.109.075114

I. INTRODUCTION

Studying the magnetotransport properties of electron systems is a valuable way to learn about their electronic structure. For example, in high-temperature cuprate superconductors, the direct-current (dc) Hall resistivity has a strong temperature (T) dependence and changes its sign in the heavily overdoped regime [1,2]. Meanwhile, the dc longitudinal resistivity in the normal state has a linear temperature dependence and exceeds the Mott-Ioffe-Regel criterion [3–5], known as strange metallicity. In an atomically thin cuprate van der Waals heterostructure during cooling, the Hall resistivity decreases and changes from positive to negative and then reverses sign again before vanishing at low temperatures. This was explained by the vortex dynamics-based description of the Hall effect in high-temperature superconductors [6]. These behaviors are incompatible with the Fermi-liquid theory of weakly interacting electrons and manifest the intricate nature of strongly correlated electron systems.

In efforts to understand the non-Fermi-liquid behaviors, various authors have calculated the magnetotransport properties of the hole-doped Hubbard model using the quantum Monte Carlo method for small square lattices [7], the dynamical mean-field theory (DMFT) approximation for hypercubic [8] and square [9–11] lattices, and an expansion formula of the Hall coefficient for small square lattices [12]. A double sign change of the T-dependent dc Hall coefficient similar to that in cuprate superconductors has been observed [8,12]. Recent numerical calculations for the square-lattice Hubbard model also revealed the T-linear dc longitudinal resistivity exceeding the Mott-Ioffe-Regel limit [13] and a T-linear electron scattering rate at low temperatures [14].

These works motivate us to further investigate the transport properties of a more complicated lattice model, the Hubbard model on a bilayer square lattice, in which electrons can form disordered interlayer singlets with a spin gap [15–17]. Accurately computing the conductivities of strongly correlated systems is notoriously difficult [18], and is frequently hindered by small lattice sizes, infinite expansion summations, or the omission of vertex corrections. We use the dimer DMFT [19] to calculate the resistivities of the hole-doped bilayer Hubbard model. The dimer DMFT works for the thermodynamic limit, but in this theory, some of the vertex corrections to the in-plane conductivities cancel out due to the neglect of in-plane nonlocal correlations [20]. However, the short-range out-of-plane correlation is still present in the Kubo bubble, enabling us to investigate how an interlayer correlation affects the transport behavior of a layered lattice system (in the normal phase), which is relevant to unconventional superconductivity [21–23].

We find that the Hall coefficient has a strong nonmonotonic T dependence at low temperatures and can change its sign twice or four times with decreasing temperature, depending on the doping level. Concomitantly, the longitudinal resistivity as a function of T acquires two plateaus that smoothly cross over to each other. These unfamiliar transport behaviors are shown to be associated with the formation of coherent interlayer singlets, which scatter off gapped collective modes arising from short-range interlayer antiferromagnetic fluctuations.

II. MODEL AND METHODS

The bilayer square-lattice Hubbard model consists of two square lattices stacked site to site. We consider only the nearest-neighbor intralayer hopping t and interlayer hopping $t_\perp$. The Hamiltonian is

$$H = -\sum_{\ell=1}^{2}\sum_{\langle \iota,\jmath\rangle,\sigma} t c^\dagger_{\ell\iota\sigma} c_{\ell\jmath\sigma} - \sum_{\iota,\sigma}(t_\perp c^\dagger_{1\iota\sigma} c_{2\iota\sigma} + \text{H.c.}) + \sum_{\ell=1}^{2}\sum_{\iota} U n_{\ell\iota\uparrow} n_{\ell\iota\downarrow}. \quad (1)$$

*yxs187@psu.edu
†jzs429@psu.edu

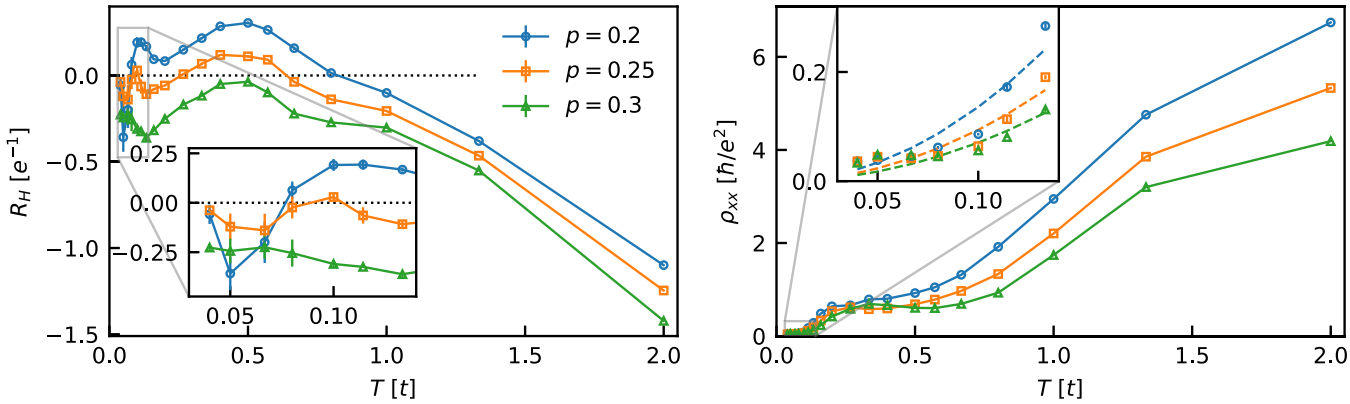

FIG. 1. Hall coefficient (left panel) and longitudinal resistivity (right panel) of the bilayer Hubbard model as functions of the temperature at various doping levels. The insets are close-up views of the lowest-temperature data. The solid lines are the guide to the eye. The dashed lines in the inset of the right panel are quadratic fits $\rho_{xx} = \text{const} \times T^2$. The error bars represent Monte Carlo sampling errors and errors arising from DMFT iterations [25], determined by four iterations starting from a converged solution.

Here, $c_{\ell\iota\sigma}$ ($c^\dagger_{\ell\iota\sigma}$) annihilates (creates) an electron of spin σ ($=\uparrow, \downarrow$) at the site ι in the layer ℓ. U is the on-site Coulomb repulsion and $n_{\ell\iota\sigma} = c^\dagger_{\ell\iota\sigma} c_{\ell\iota\sigma}$ is the electron number operator. We choose $t_\perp = 1.2t$ and $U = 10t$, which are relevant to the material VO_2 [15], a prototypical strongly correlated oxide with the vanadium dimer as the basic unit [24]. In the DMFT, we consider an interlayer dimer embedded in a self-consistent noninteracting electron bath, thereby fully taking into account the short-range interlayer electron correlation (see Appendix A for a detailed description of the calculation and postprocessing methods). In this case, the vertex corrections to the conductivity should not completely cancel, because the self-energy is not fully local. We will neglect this part of the vertex corrections and approximate the longitudinal and Hall dc conductivities (sheet conductances) by the Kubo bubble (see Appendix B for the derivation of the Kubo formulas).

III. TRANSPORT COEFFICIENTS

Figure 1 shows the calculated Hall coefficient R_H and longitudinal resistivity ρ_{xx} as functions of the temperature at various hole doping levels $p = 1 - \sum_\sigma \langle n_{\ell\iota\sigma} \rangle$. For $T \gtrsim 0.1t$, the T dependence of R_H is similar for all doping levels shown, but R_H shifts downward with increasing doping. In this temperature range, as T increases, R_H decreases in $0.1t \lesssim T \lesssim 0.13t$, then increases in $0.13t \lesssim T \lesssim 0.5t$, and then decreases again for $T \gtrsim 0.5t$. In $0.67t \lesssim T \lesssim 1t$, $R_H(T)$ changes more slowly with increasing doping and becomes almost flat at $p = 0.3$. Depending on the doping level, R_H can be totally below zero ($p = 0.3$), or change sign once ($p = 0.2$) or three times ($p = 0.25$) in this range $T \gtrsim 0.1t$.

For $T \lesssim 0.1t$, the behaviors of $R_H(T)$ at different doping levels are radically different. In this temperature range, the T dependence of R_H quickly weakens with increasing doping. At $p = 0.2$ and $p = 0.25$, R_H changes sign once due to its strong dependence on T. But for a heavier doping $p = 0.3$, $R_H(T)$ is almost a negative constant. Therefore, the total number of times $R_H(T)$ changes its sign counts to zero at $p = 0.3$, two at $p = 0.2$, and as many as four at $p = 0.25$, in contrast to the single or double sign reversal normally observed in high-temperature superconductors [2,6,26] and the single-orbital Hubbard model [8,12].

The longitudinal resistivity $\rho_{xx}(T)$ also shows unfamiliar behavior (Fig. 1, right panel). There are two temperature ranges, $0.26t \lesssim T \lesssim 0.5t$ and $T \lesssim 0.1t$, where $\rho_{xx}(T)$ is almost constant, and these ranges become broader for heavier doping. Especially at low temperatures, $\rho_{xx}(T)$ deviates significantly from the quadratic fits $\rho_{xx} = \text{const} \times T^2$ expected for a Fermi liquid (Fig. 1, right panel, inset). Nevertheless, the quadratic fit is improved for heavier doping, along with the weaker T dependence of R_H for heavier doping (Fig. 1, left panel, inset), demonstrating that the system at low temperatures approaches the Fermi-liquid phase as doping increases. The constant value of ρ_{xx} in $T \lesssim 0.1t$ does not change much as the doping level is varied, whereas at high temperatures, ρ_{xx} exceeds the Mott-Ioffe-Regel limit ($\sim\sqrt{2\pi}\hbar/e^2 \approx 2.5\hbar/e^2$ [5]) and is lower for heavier doping consistent with more charge carriers.

IV. MECHANISMS

To understand the anomalous behaviors of the Hall coefficient and longitudinal resistivity, we plot in Fig. 2 the total single-particle excitation spectra $A(\mathbf{k}, \omega)$ and densities of states $A(\omega) = \sum_{\mathbf{k}} A(\mathbf{k}, \omega)/N$ at various temperatures for $p = 0.25$. The noninteracting band structure is also superimposed (dotted lines). In the noninteracting limit, at light doping, the bonding (lower-lying) band has a hole pocket at the M point and the antibonding (higher-lying) band has a smaller electron pocket at the Γ point, which is the case for $p = 0.25$. At heavy doping, both the bonding and antibonding bands have an electron pocket at the Γ point.

At a high temperature $T = 2t$, the spectrum is highly incoherent and continuous, showing only two broad Hubbard bands centered around $\omega = -1t$ and $\omega = 10t$, respectively, with a pseudogap in between. Charge excitation across this pseudogap produces a negative R_H [8]. As T is lowered to $1t$, the spectrum near the Fermi level becomes more coherent, and the peak of the density of states of the lower Hubbard band moves to a higher energy. Fewer electrons are excited

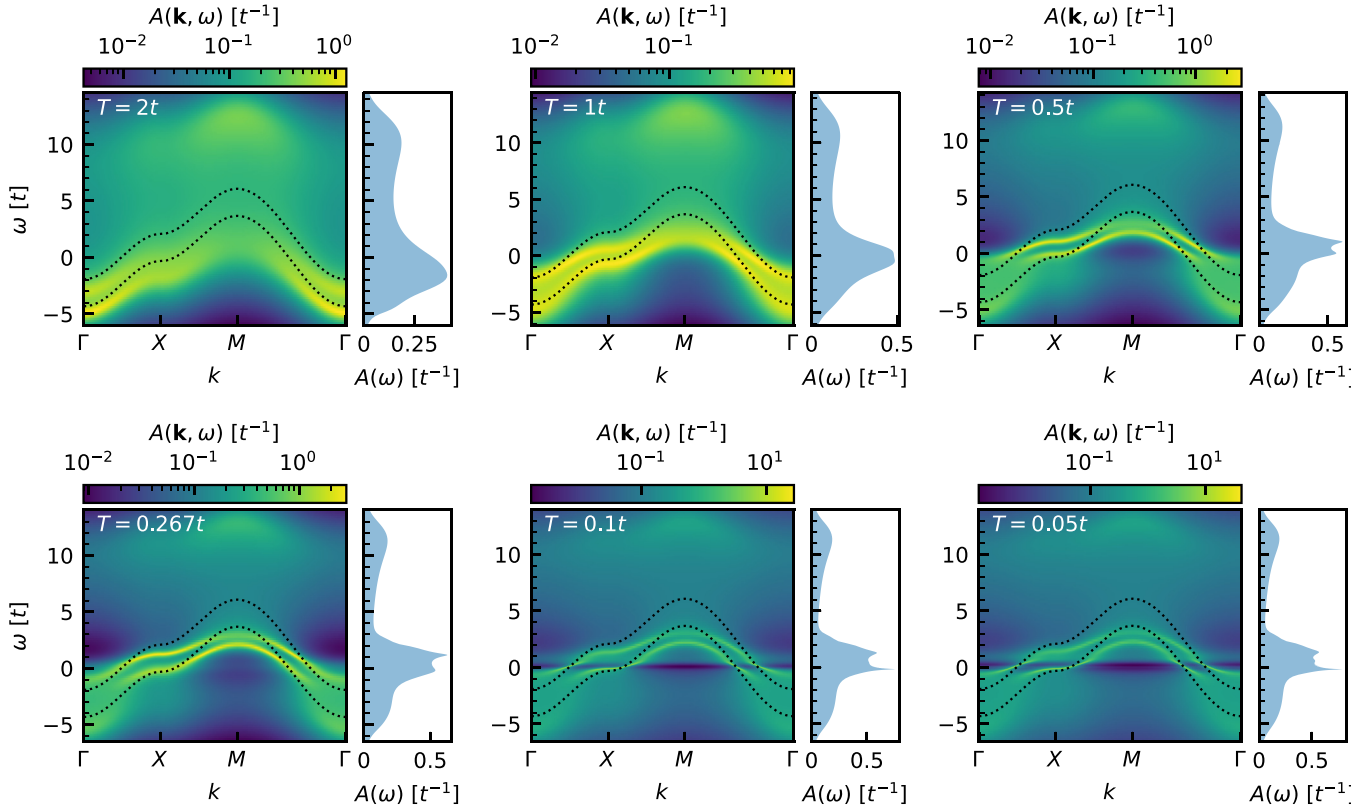

FIG. 2. Single-particle excitation spectra $A(\mathbf{k},\omega)$ along a path connecting high-symmetry reciprocal points, and corresponding densities of states $A(\omega)$ at indicated temperatures for $p = 0.25$. The black dotted lines are the noninteracting bands for the same doping. The Fermi level lies at $\omega = 0$.

onto the upper Hubbard band, leading to a more holelike R_H, that is, a larger R_H.

At a moderate temperature $T = 0.5t$, two dispersive quasiparticle bands develop near and above the Fermi level, whereas the two incoherent Hubbard bands persist. The quasiparticle bands are renormalized by the Kondo screening [15] to be approximately twice as narrow as their noninteracting counterparts. To see the interlayer Kondo screening, we show in the left panel of Fig. 3 the nearest-neighbor interlayer spin correlation function $\langle S^z_{1t} S^z_{2t}\rangle$ as a function of temperature at various doping levels, where $S^z_{\ell t} = n_{\ell t\uparrow} - n_{\ell t\downarrow}$ is the spin density operator. The neighboring interlayer spins do tend to be antiparallel, resulting in mutual screening. The singlet correlation strength peaks at a nonzero temperature that increases with increasing doping. For $T \lesssim 0.5t$, the singlet correlation strength is significant [14] and considerably larger than that at $T = 2t$, compatible with the observed crossover from the totally incoherent spectrum at $T = 2t$ to the renormalized

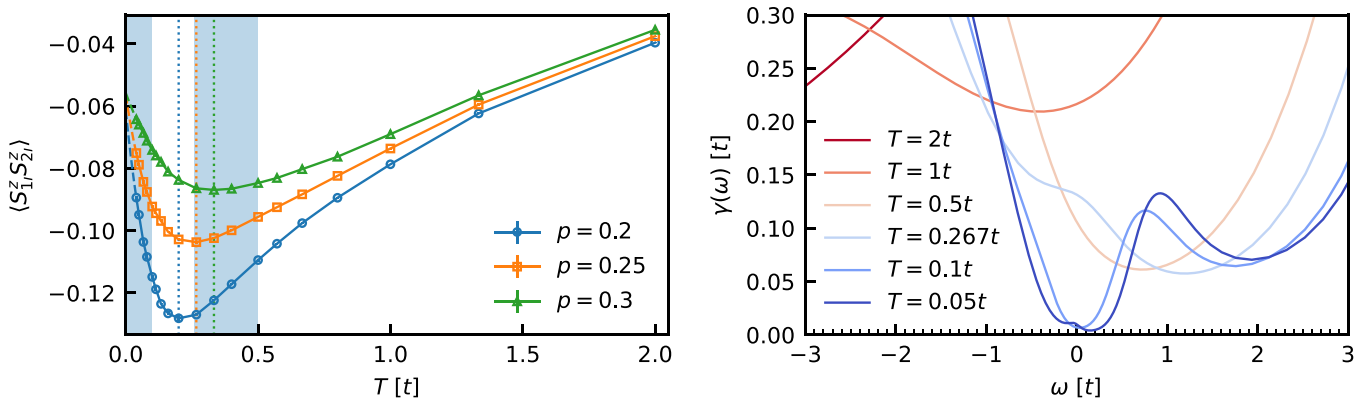

FIG. 3. Left panel: Interlayer singlet correlation as a function of the temperature at various doping levels. Vertical dotted lines mark the temperatures of the maximum correlation strength, T_m. Dashed lines are extrapolations to zero temperature by fitting the data for $T < T_m$ to cubic functions. Shaded patches indicate the approximate T regions of the two resistivity plateaus. Right panel: Scattering rate spectrum (see text) in the low-energy range at $p = 0.25$ for the various temperatures in correspondence to Fig. 2.

coherent bands at $T = 0.5t$, which can thus be viewed as interlayer singlet bands [15]. Compared to the spectrum at $T = 1t$, the hole pocket at the M point is relatively well defined owing to the coherent singlet bands, while the electron pocket at the Γ point remains incoherent, leading to an overall positive R_H (Fig. 1, left panel).

As T is lowered from $0.5t$ to $0.267t$, the spectral function does not change much. In particular, the smearing of the quasiparticle bands at these two temperatures is similar, both being $\sim 0.5t$ wide and having a spectral weight of $\sim 3t^{-1}$. This is consistent with the Kondo resonance, in which the width and height of the resonance peak are temperature independent and are only determined by one energy scale, the Kondo temperature [27]. In this temperature range, T is less than the smearing width of the quasiparticle bands, resulting in approximately T-constant resistivity (Fig. 1, right panel) reminiscent of resistivity saturation in the Kondo problem. There are two slight, yet visible changes in the spectral function as T is lowered from $0.5t$ to $0.267t$. One is that the electron pocket at the Γ point becomes more well defined and deeper on the way to the complete formation of the coherent singlet bands. The other is the appearance of a weak incoherent flat band with a smearing width of $\sim 1t$ at the Fermi level, which hosts electrons. These two changes tend to reduce R_H (Fig. 1, left panel).

At a relatively low temperature $T = 0.1t$, a small single-particle gap *in the incoherent spectrum* ($\sim 0.4t$) opens at the Fermi level. Concomitantly, the coherent singlet bands within the incoherent spectrum gap (spectral weight $\sim 30t^{-1}$) become much sharper and flatter than those at $T = 0.267t$ (spectral weight $\sim 3t^{-1}$). This results in a very sharp peak in the density of states at the Fermi level, which is the manifestation of a strong Kondo resonance. The opening of the gap in the incoherent spectrum depopulates the upper Hubbard band, and the hole pocket of the well-defined singlet bands is larger than its electron pocket, resulting in an increase in $R_H(T)$ from $T \simeq 0.13t$ to $T \simeq 0.1t$ (Fig. 1, left panel).

As T decreases from $0.1t$ to $0.05t$, the quasiparticle bands again remain almost unchanged, with a $\sim 0.1t$ smearing width and $\sim 30t^{-1}$ spectral weight at the Fermi level. Therefore, the resistivity in $T \lesssim 0.1t$ should also be approximately temperature independent (Fig. 1, right panel). The two plateaus in $\rho_{xx}(T)$ are smoothly connected by a crossover spanning from $T \simeq 0.1t$ to $T \simeq 0.26t$. At $T = 0.05t$, a flat band (not the quasiparticle band) with weak intensity ($\sim 0.1t^{-1}$) appears at the Fermi level, which hosts electrons leading to a decrease in $R_H(T)$ from $T \simeq 0.1t$ to $T \simeq 0.05t$ (Fig. 1, left panel).

The non-Fermi-liquid behavior down to very low temperatures also has a manifestation in the interlayer spin correlation, which does not vanish at zero temperature (Fig. 3, left panel). Instead, the singlet correlation extrapolated to zero temperature is ~ -0.06, which is very close to the nearest-neighbor spin correlation responsible for the non-Fermi-liquid scattering in the overdoped monolayer square-lattice Hubbard model at low temperatures [14]. A dynamical cluster approximation study of the doped bilayer Hubbard model suggested that there exists non-Fermi-liquid behavior even in the absence of a finite scattering rate at vanishing temperature, attributed to short-range interlayer antiferromagnetic fluctuation [28]. This observation is consistent with our results, nevertheless we showed that the resulting non-Fermi-liquid behavior is not the T-linear resistivity but a resistivity plateau.

To show where the Kondo saturation comes from, we depict in the right panel of Fig. 3 the scattering rate spectrum, $\gamma(\omega) = \{\sum_{o,\sigma}[-\mathrm{Im}\,\Sigma_{o\sigma}(\omega)]^{-1}\}^{-1}$ [14], where $\Sigma_{o\sigma}(\omega)$ is the oth diagonal element of the diagonalized self-energy matrix of spin σ in the layer-index space. At the lowest temperature shown, $T = 0.05t$, $\gamma(\omega)$ has two peaks in the low-energy range located at $\omega \simeq 0$ and $\omega \simeq 0.9t$, respectively, which are separated by a gap spanning $0.05t \lesssim \omega \lesssim 0.3t \equiv \omega_g$. These two peaks are absent in the DMFT result of the single-orbital Hubbard model [following the Fermi-liquid behavior at low temperatures, $\gamma(\omega) \sim \omega^2$ at small ω [19,29]] and represent two low-energy scattering modes arising from short-range interlayer antiferromagnetic fluctuations. The zero-energy mode should be the simultaneous flip of spins in the inert interlayer singlet costing no energy, while the second mode should be the flip of a single spin in the singlet. There is also a pseudogap at $\omega \simeq 2t$ that separates the second scattering mode and a broad peak at a high energy $\omega \simeq 7.8t$ (not shown) corresponding to scattering off doubly-occupied-site states.

The zero-energy scattering mode is responsible for nonzero resistivity at vanishing temperatures. For $T \lesssim 0.1t \simeq \omega_g/3$, electrons near the Fermi level thermally fluctuate so weakly that they cannot cross the gap to scatter off the second scattering mode [30]. Therefore, the scattering rate $\gamma(0)$ at $T = 0.1t$ saturates and is close to that at $T = 0.05t$, leading to the lower resistivity plateau at $T \lesssim 0.1t$. Similarly, the pseudogap renders the scattering rates $\gamma(0)$ at $T \simeq 0.267t$ and $T \simeq 0.5t$ near and both close to that of the second scattering mode [$\gamma(0.9t)$ at $T = 0.05t$], forming the higher resistivity plateau at $0.26t \lesssim T \lesssim 0.5t$. But because the pseudogap is not a genuine gap, the higher resistivity plateau is not as flat as the lower resistivity plateau (Fig. 1, right panel). For heavier doping, the Kondo resonance peak will get wider [19,29], i.e., the (pseudo)gap in $\gamma(\omega)$ will become wider, resulting in wider resistivity plateaus (Fig. 1, right panel). This reconciliation between the frequency dependence of γ at the lowest temperature shown and the temperature dependence of ρ_{xx} also increases our confidence in the accuracy of the analytical continuation of self-energies.

V. CONCLUSIONS AND DISCUSSIONS

In conclusion, we have calculated the Hall coefficient and longitudinal resistivity of the hole-doped bilayer Hubbard model and found that its transport properties are very different from those of the monolayer or single-orbital Hubbard model. The Hall coefficient has a strong nonmonotonic dependence on temperature at low temperatures, and it can change sign four times for some range of doping. The resistivity at low temperatures is not linear in temperature as that of strange metals or quadratic in temperature as that of Fermi liquids. Rather, it exhibits two plateaus with a smooth crossover between them. These anomalous transport behaviors can be traced back to the formation of coherent interlayer singlets, which scatter off gapped collective modes arising from short-range interlayer antiferromagnetic fluctuations.

The vertex corrections to the dc conductivities could be significant in low-dimensional systems. The evaluation for the

monolayer Hubbard model may hint at the effect of the vertex corrections in the bilayer Hubbard model. At high temperatures, the inclusion of the vertex corrections shifts $\rho_{xx}(T)$ downward but preserves its temperature dependence [31,32], whereas at low temperatures it only slightly modulates ρ_{xx} for moderate doping levels [33,34]. Neither does it alter the trend of $R_H(T)$ [7,8,12]. Compared to the monolayer model, the bilayer Hubbard model should host even smaller vertex corrections due to its larger coordination number. Therefore, we do not expect the vertex corrections to give rise to resistivity behaviors qualitatively different from our conclusions. Our results could stimulate future works to calculate the transport coefficients of the bilayer Hubbard model more precisely by incorporating the vertex corrections, which could be possibly done within the cluster extension of the DMFT [35], the dynamical vertex approximation [36,37], or by approximating the vertex function with its molecular limit [38].

ACKNOWLEDGMENTS

We thank Jakša Vučičević, Jainendra Jain, and Fei Yang for useful discussions. This work was supported as part of the Computational Materials Sciences Program funded by the U.S. Department of Energy, Office of Science, Basic Energy Sciences, under Award No. DE-SC0020145. J.S. was supported by the U.S. Department of Energy, Office of Basic Energy Sciences, under Grant No. DE-SC-0005042. This research used resources of the National Energy Research Scientific Computing Center, a DOE Office of Science User Facility supported by the Office of Science of the U.S. Department of Energy under Contract No. DE-AC02-05CH11231 using NERSC Award No. BES-ERCAP0027694.

APPENDIX A: SIMULATION METHODS

We use the continuous-time auxiliary-field Monte Carlo method (CT-AUX) [39,40] to solve the corresponding quantum impurity problem. In the CT-AUX, we directly measure the Green's function and its stochastic error in the Matsubara frequency domain. We then employ the recently developed maximum quantum entropy method (MQEM) [41] to analytically continue the self-energy matrix to the real-frequency axis. Unlike in most previous maximum entropy calculations in which the analytical continuation was performed for data in the imaginary time domain, we analytically continue the self-energy in the Matsubara frequency domain [41], which is directly measured in the CT-AUX. We decompose the self-energy into a static part, which is obtained by analytical asymptotic expansion, and a dynamical part, which is analytically continued directly. We utilize a robust standard for determining α, the entropy weight in the MQEM [42]. The reliability of this standard does not depend on the proximity between the spectrum and the default model, so very little prior information is needed from the spectrum to obtain good results. We also adopted cubic splines with nonuniform real-frequency grids to help resolve small features [42]. These strategies have been proven to yield quite accurate results that almost perfectly match the exact spectra [42].

APPENDIX B: KUBO FORMULAS

To derive the Kubo formulas for the conductivities of the bilayer Hubbard model, we follow the derivation for the monolayer Hubbard model [20] and start from the Hamiltonian with a constant out-of-plane magnetic field $B_z\mathbf{e}_z = \nabla\times\mathbf{A}$ and an infinitesimal uniform in-plane electric field $\mathbf{E} = \dot{\mathbf{A}}^{\text{ext}}$,

$$H = -t\sum_{\ell,\mathbf{r},\mathbf{u}\in\{\mathbf{a}_x,\mathbf{a}_y\},\sigma}\left[e^{i(f_{\mathbf{r},\mathbf{r}+\mathbf{u}}+e\mathbf{A}^{\text{ext}}_{\mathbf{r}}\cdot\mathbf{u}/\hbar)}c^\dagger_{\ell,\mathbf{r},\sigma}c_{\ell,\mathbf{r}+\mathbf{u},\sigma}+\text{H.c.}\right] - t_\perp\sum_{\mathbf{r},\sigma}(c^\dagger_{1,\mathbf{r},\sigma}c_{2,\mathbf{r},\sigma}+\text{H.c.}) + U\sum_{\ell,\mathbf{r},\sigma}n_{\ell,\mathbf{r},\uparrow}n_{\ell,\mathbf{r},\downarrow}, \quad \text{(B1)}$$

where $f_{\mathbf{r},\mathbf{r}'} = (e/\hbar)\int_{\mathbf{r}}^{\mathbf{r}'}\mathbf{A}\cdot d\mathbf{r}$ is a part of the Peierls phase, $\mathbf{r}$ is the in-plane position vector of a site, and $\mathbf{a}_x$ and $\mathbf{a}_y$ are the in-plane lattice constants. Note that within the nearest hopping approximation, $\mathbf{A}$ and $\mathbf{A}^{\text{ext}}$ only enter the in-plane hopping terms in the Hamiltonian Eq. (B1) because they are perpendicular to the out-of-plane direction. Therefore, the current density operator along an in-plane direction $\eta\in\{x,y\}$,

$$j^\eta_{\mathbf{r}} = -\frac{1}{a^2c}\frac{\partial H}{\partial A^{\eta,\text{ext}}_{\mathbf{r}}}\bigg|_{\mathbf{A}^{\text{ext}}\to\mathbf{0}} \quad \text{(B2)}$$

$$= \frac{ite}{\hbar ac}\sum_{\ell,\sigma}e^{if_{\mathbf{r},\mathbf{r}+\mathbf{a}_\eta}}c^\dagger_{\ell,\mathbf{r},\sigma}c_{\ell,\mathbf{r}+\mathbf{a}_\eta,\sigma}+\text{H.c.}, \quad \text{(B3)}$$

differs from that of the monolayer Hubbard model only by an additional summation over the layer index ℓ, where c is the distance between the two layers. It does not explicitly contain $t_\perp$. Then we have for the Kubo bubble (without the vertex corrections) of the current-current correlation function,

$$\Lambda^{\eta\eta',\text{bubble}}_{\mathbf{r},\mathbf{r}'}(\tau) = \left\langle j^\eta_{\mathbf{r}}(\tau)j^{\eta'}_{\mathbf{r}'}(0)\right\rangle_{\text{bubble}} - \left\langle j^\eta_{\mathbf{r}}\right\rangle\left\langle j^{\eta'}_{\mathbf{r}'}\right\rangle \quad \text{(B4)}$$

$$= -\frac{t^2e^2}{\hbar^2a^2c^2}\sum_{\ell,\ell',\sigma,\sigma'}\sum_{b,b'\in\{0,1\}}(-1)^{b+b'}C^b(e^{if_{\mathbf{r},\mathbf{r}+\mathbf{a}_\eta}})C^{b'}(e^{if_{\mathbf{r}',\mathbf{r}'+\mathbf{a}_{\eta'}}}) \times\left\langle c^\dagger_{\ell,\mathbf{r}+b\mathbf{a}_\eta,\sigma}(\tau^+)c_{\ell,\mathbf{r}+(1-b)\mathbf{a}_\eta,\sigma}(\tau)c^\dagger_{\ell',\mathbf{r}'+b'\mathbf{a}_{\eta'},\sigma'}(0^+)c_{\ell',\mathbf{r}'+(1-b')\mathbf{a}_{\eta'},\sigma'}(0)\right\rangle_{\text{bubble}} - \left\langle j^\eta_{\mathbf{r}}\right\rangle\left\langle j^{\eta'}_{\mathbf{r}'}\right\rangle \quad \text{(B5)}$$

$$= \frac{t^2e^2}{\hbar^2a^2c^2}\sum_{\ell,\ell',\sigma}\sum_{b,b'\in\{0,1\}}(-1)^{b+b'}C^b(e^{if_{\mathbf{r},\mathbf{r}+\mathbf{a}_\eta}})C^{b'}(e^{if_{\mathbf{r}',\mathbf{r}'+\mathbf{a}_{\eta'}}})G_{\ell,\ell',\mathbf{r}+(1-b)\mathbf{a}_\eta,\mathbf{r}'+b'\mathbf{a}_{\eta'},\sigma}(\tau)G_{\ell',\ell,\mathbf{r}'+(1-b')\mathbf{a}_{\eta'},\mathbf{r}+b\mathbf{a}_\eta,\sigma}(-\tau) \quad \text{(B6)}$$

$$= \frac{t^2e^2}{\hbar^2a^2c^2}\sum_{\sigma}\sum_{b,b'\in\{0,1\}}(-1)^{b+b'}C^b(e^{if_{\mathbf{r},\mathbf{r}+\mathbf{a}_\eta}})C^{b'}(e^{if_{\mathbf{r}',\mathbf{r}'+\mathbf{a}_{\eta'}}})\text{Tr}[\hat{G}_{\mathbf{r}+(1-b)\mathbf{a}_\eta,\mathbf{r}'+b'\mathbf{a}_{\eta'},\sigma}(\tau)\hat{G}_{\mathbf{r}'+(1-b')\mathbf{a}_{\eta'},\mathbf{r}+b\mathbf{a}_\eta,\sigma}(-\tau)], \quad \text{(B7)}$$

where τ is imaginary time, $C(\cdot)$ is the complex conjugation operator with $C^0 = 1$, and G is the Green's function. Compared to Eq. (B7), $\Lambda^{\eta\eta',\text{bubble}}_{\mathbf{r},\mathbf{r}'}(\tau)$ of the monolayer Hubbard model [20] is just Eq. (B7) with its second line replaced by

$$G_{\mathbf{r}+(1-b)\mathbf{a}_\eta,\mathbf{r}'+b'\mathbf{a}_{\eta'},\sigma}(\tau)G_{\mathbf{r}'+(1-b')\mathbf{a}_{\eta'},\mathbf{r}+b\mathbf{a}_\eta,\sigma}(-\tau), \tag{B8}$$

showing that the current-current correlation function without the vertex corrections of the bilayer Hubbard model is just a matrix-multiplication counterpart of that of the monolayer Hubbard model. Therefore, the longitudinal and Hall dc conductivities (sheet conductances) without the vertex corrections in a vanishing out-of-plane magnetic field $B_z \to 0$ can be directly extended from those for the monolayer Hubbard model [8,29,43],

$$\sigma_{xx} = \frac{e^2\pi}{\hbar N}\sum_{\mathbf{k},\sigma}\left(\frac{\partial\epsilon_\mathbf{k}}{\partial k_x}\right)^2\int \mathrm{d}\omega \mathrm{Tr}[\hat{A}_{\mathbf{k}\sigma}(\omega)^2]\left[-\frac{\mathrm{d}n_F(\omega)}{\mathrm{d}\omega}\right], \tag{B9}$$

$$\frac{\sigma_{xy}}{B_z} = \frac{2\pi^2 e^3 a^2}{3\hbar^2 N}\sum_{\mathbf{k},\sigma}\left(\frac{\partial\epsilon_\mathbf{k}}{\partial k_x}\right)^2\frac{\partial^2\epsilon_\mathbf{k}}{\partial k_y^2}\int \mathrm{d}\omega \mathrm{Tr}[\hat{A}_{\mathbf{k}\sigma}(\omega)^3]\left[-\frac{\mathrm{d}n_F(\omega)}{\mathrm{d}\omega}\right]. \tag{B10}$$

Here, N is the number of unit cells in the lattice. $\mathbf{k} = (k_x, k_y)$ is the reciprocal vector in the first Brillouin zone. $n_F(\omega) = (1 + e^{\hbar\omega/T})^{-1}$ is the Fermi distribution function. The energy of the bonding or antibonding band up to a constant shift is $\epsilon_\mathbf{k} = -2t(\cos k_x + \cos k_y)$. $\hat{A}$ is the spectral function, which is a matrix in the layer-index space. The interlayer correlation is incorporated through the off-diagonal elements of $\hat{A}$.

The longitudinal resistivity and the Hall coefficient are related to the conductivities by $\rho_{xx} = \sigma_{xx}^{-1}$ and $R_H = \sigma_{xy}/(B_z\sigma_{xx}^2)$, respectively.

[1] H. Y. Hwang, B. Batlogg, H. Takagi, H. L. Kao, J. Kwo, R. J. Cava, J. J. Krajewski, and W. F. Peck, Scaling of the temperature dependent Hall effect in $La_{2-x}Sr_xCuO_4$, Phys. Rev. Lett. **72**, 2636 (1994).

[2] I. Tsukada and S. Ono, Negative Hall coefficients of heavily overdoped $La_{2-x}Sr_xCuO_4$, Phys. Rev. B **74**, 134508 (2006).

[3] M. Gurvitch and A. T. Fiory, Resistivity of $La_{1.825}Sr_{0.175}CuO_4$ and $YBa_2Cu_3O_7$ to 1100 K: Absence of saturation and its implications, Phys. Rev. Lett. **59**, 1337 (1987).

[4] Y. Ando, S. Komiya, K. Segawa, S. Ono, and Y. Kurita, Electronic phase diagram of high-T_c cuprate superconductors from a mapping of the in-plane resistivity curvature, Phys. Rev. Lett. **93**, 267001 (2004).

[5] O. Gunnarsson, M. Calandra, and J. E. Han, Colloquium: Saturation of electrical resistivity, Rev. Mod. Phys. **75**, 1085 (2003).

[6] S. Y. F. Zhao, N. Poccia, M. G. Panetta, C. Yu, J. W. Johnson, H. Yoo, R. Zhong, G. D. Gu, K. Watanabe, T. Taniguchi, S. V. Postolova, V. M. Vinokur, and P. Kim, Sign-reversing Hall effect in atomically thin high-temperature $Bi_{2.1}Sr_{1.9}CaCu_{2.0}O_{8+\delta}$ superconductors, Phys. Rev. Lett. **122**, 247001 (2019).

[7] F. F. Assaad and M. Imada, Hall coefficient for the two-dimensional Hubbard model, Phys. Rev. Lett. **74**, 3868 (1995).

[8] E. Lange and G. Kotliar, Magnetotransport in the doped Mott insulator, Phys. Rev. B **59**, 1800 (1999).

[9] A. A. Markov, G. Rohringer, and A. N. Rubtsov, Robustness of the topological quantization of the Hall conductivity for correlated lattice electrons at finite temperatures, Phys. Rev. B **100**, 115102 (2019).

[10] J. Vučičević and R. Žitko, Universal magnetic oscillations of dc conductivity in the incoherent regime of correlated systems, Phys. Rev. Lett. **127**, 196601 (2021).

[11] E. Z. Kuchinskii, N. A. Kuleeva, D. I. Khomskii, and M. V. Sadovskii, Hall effect in a doped Mott insulator: DMFT approximation, JETP Lett. **115**, 402 (2022).

[12] W. O. Wang, J. K. Ding, B. Moritz, E. W. Huang, and T. P. Devereaux, DC Hall coefficient of the strongly correlated Hubbard model, npj Quantum Mater. **5**, 51 (2020).

[13] E. W. Huang, R. Sheppard, B. Moritz, and T. P. Devereaux, Strange metallicity in the doped Hubbard model, Science **366**, 987 (2019).

[14] W. Wú, X. Wang, and A.-M. Tremblay, Non-Fermi liquid phase and linear-in-temperature scattering rate in overdoped two-dimensional Hubbard model, Proc. Natl. Acad. Sci. USA **119**, e2115819119 (2022).

[15] O. Nájera, M. Civelli, V. Dobrosavljević, and M. J. Rozenberg, Resolving the VO_2 controversy: Mott mechanism dominates the insulator-to-metal transition, Phys. Rev. B **95**, 035113 (2017).

[16] O. Nájera, M. Civelli, V. Dobrosavljević, and M. J. Rozenberg, Multiple crossovers and coherent states in a Mott-Peierls insulator, Phys. Rev. B **97**, 045108 (2018).

[17] Y. Mou, R. Mondaini, and R. T. Scalettar, Bilayer Hubbard model: Analysis based on the fermionic sign problem, Phys. Rev. B **106**, 125116 (2022).

[18] A. Auerbach, Hall number of strongly correlated metals, Phys. Rev. Lett. **121**, 066601 (2018).

[19] A. Georges, G. Kotliar, W. Krauth, and M. J. Rozenberg, Dynamical mean-field theory of strongly correlated fermion systems and the limit of infinite dimensions, Rev. Mod. Phys. **68**, 13 (1996).

[20] J. Vučičević and R. Žitko, Electrical conductivity in the Hubbard model: Orbital effects of magnetic field, Phys. Rev. B **104**, 205101 (2021).

[21] T. A. Maier and D. J. Scalapino, Pair structure and the pairing interaction in a bilayer Hubbard model for unconventional superconductivity, Phys. Rev. B **84**, 180513(R) (2011).

[22] S. Karakuzu, S. Johnston, and T. A. Maier, Superconductivity in the bilayer Hubbard model: Two Fermi surfaces are better than one, Phys. Rev. B **104**, 245109 (2021).

[23] A. Iwano and Y. Yamaji, Superconductivity in bilayer t-t' Hubbard models, J. Phys. Soc. Jpn. **91**, 094702 (2022).

[24] S. Biermann, A. Poteryaev, A. I. Lichtenstein, and A. Georges, Dynamical singlets and correlation-assisted Peierls transition in VO_2, Phys. Rev. Lett. **94**, 026404 (2005).

[25] E. Gull, P. Werner, A. Millis, and M. Troyer, Performance analysis of continuous-time solvers for quantum impurity models, Phys. Rev. B **76**, 235123 (2007).

[26] D. Li, K. Lee, B. Y. Wang, M. Osada, S. Crossley, H. R. Lee, Y. Cui, Y. Hikita, and H. Y. Hwang, Superconductivity in an infinite-layer nickelate, Nature (London) **572**, 624 (2019).

[27] G. D. Mahan, *Many-Particle Physics*, 3rd ed. (Klumer Academic/Plenum Publishers, New York, 2000).

[28] H. Lee, Y.-Z. Zhang, H. O. Jeschke, and R. Valentí, Competition between band and Mott insulators in the bilayer Hubbard model: A dynamical cluster approximation study, Phys. Rev. B **89**, 035139 (2014).

[29] T. Pruschke, M. Jarrell, and J. Freericks, Anomalous normal-state properties of high-T_c superconductors: Intrinsic properties of strongly correlated electron systems? Adv. Phys. **44**, 187 (1995).

[30] S. A. Hartnoll and A. P. Mackenzie, Colloquium: Planckian dissipation in metals, Rev. Mod. Phys. **94**, 041002 (2022).

[31] J. Vučičević, J. Kokalj, R. Žitko, N. Wentzell, D. Tanasković, and J. Mravlje, Conductivity in the square lattice Hubbard model at high temperatures: Importance of vertex corrections, Phys. Rev. Lett. **123**, 036601 (2019).

[32] A. Vranić, J. Vučičević, J. Kokalj, J. Skolimowski, R. Žitko, J. Mravlje, and D. Tanasković, Charge transport in the Hubbard model at high temperatures: Triangular versus square lattice, Phys. Rev. B **102**, 115142 (2020).

[33] N. Lin, E. Gull, and A. J. Millis, Optical conductivity from cluster dynamical mean-field theory: Formalism and application to high-temperature superconductors, Phys. Rev. B **80**, 161105(R) (2009).

[34] A. Mu, Z. Sun, and A. J. Millis, Optical conductivity of the two-dimensional Hubbard model: Vertex corrections, emergent Galilean invariance, and the accuracy of the single-site dynamical mean field approximation, Phys. Rev. B **106**, 085142 (2022).

[35] N. Lin, E. Gull, and A. J. Millis, Two-particle response in cluster dynamical mean-field theory: Formalism and application to the Raman response of high-temperature superconductors, Phys. Rev. Lett. **109**, 106401 (2012).

[36] G. Rohringer, H. Hafermann, A. Toschi, A. A. Katanin, A. E. Antipov, M. I. Katsnelson, A. I. Lichtenstein, A. N. Rubtsov, and K. Held, Diagrammatic routes to nonlocal correlations beyond dynamical mean field theory, Rev. Mod. Phys. **90**, 025003 (2018).

[37] J. Kaufmann, C. Eckhardt, M. Pickem, M. Kitatani, A. Kauch, and K. Held, Self-consistent ladder dynamical vertex approximation, Phys. Rev. B **103**, 035120 (2021).

[38] P. Thunström, O. Gunnarsson, S. Ciuchi, and G. Rohringer, Analytical investigation of singularities in two-particle irreducible vertex functions of the Hubbard atom, Phys. Rev. B **98**, 235107 (2018).

[39] E. Gull, P. Werner, O. Parcollet, and M. Troyer, Continuous-time auxiliary-field Monte Carlo for quantum impurity models, Europhys. Lett. **82**, 57003 (2008).

[40] E. Gull, A. J. Millis, A. I. Lichtenstein, A. N. Rubtsov, M. Troyer, and P. Werner, Continuous-time Monte Carlo methods for quantum impurity models, Rev. Mod. Phys. **83**, 349 (2011).

[41] J.-H. Sim and M. J. Han, Maximum quantum entropy method, Phys. Rev. B **98**, 205102 (2018).

[42] D. Bergeron and A.-M. S. Tremblay, Algorithms for optimized maximum entropy and diagnostic tools for analytic continuation, Phys. Rev. E **94**, 023303 (2016).

[43] P. Voruganti, A. Golubentsev, and S. John, Conductivity and Hall effect in the two-dimensional Hubbard model, Phys. Rev. B **45**, 13945 (1992).